Breaking the symmetry of a wavy channel alters the route to chaotic flow

Mohammad Hossein Doranehgard*
Department of Mechanical and Aerospace Engineering, The Hong Kong University of Science and Technology, Clear Water Bay, Hong Kong

Nader Karimi
School of Engineering and Materials Science, Queen Mary University of London, London E1 4NS, United Kingdom

Iman Borazjani
J. Mike Walker 66 Department of Mechanical Engineering, Texas A&M University, College Station, Texas 77840, USA

Larry K. B. Li†
Department of Mechanical and Aerospace Engineering, The Hong Kong University of Science and Technology, Clear Water Bay, Hong Kong

(Received 11 May 2023; accepted 14 March 2024; published 4 April 2024)

We numerically explore the two-dimensional, incompressible, isothermal flow through a wavy channel, with a focus on how the channel geometry affects the routes to chaos at Reynolds numbers between 150 and 1000. We find that (i) the period-doubling route arises in a symmetric channel, (ii) the Ruelle-Takens-Newhouse route arises in an asymmetric channel, and (iii) the type-II intermittency route arises in both asymmetric and semiwavy channels. We also find that the flow through the semiwavy channel evolves from a quasiperiodic torus to an unstable invariant set (chaotic saddle), before eventually settling on a period-1 limit-cycle attractor. This study reveals that laminar channel flow at elevated Reynolds numbers can exhibit a variety of nonlinear dynamics. Specifically, it highlights how breaking the symmetry of a wavy channel can not only influence the critical Reynolds number at which chaos emerges, but also diversify the types of bifurcation encountered en route to chaos itself.

DOI: 10.1103/PhysRevE.109.045103

I. INTRODUCTION

From combustion [1,2] to heat transfer [3–6] to biomechanics [7,8], wavy or corrugated channels have received significant attention from researchers owing to their ability to enhance mass, momentum, and heat exchange. The presence of corrugations in a channel can disrupt the growth of boundary layers, resulting in flow separation and reattachment, which can in turn enhance the mixing of the near-wall fluid with the core fluid. Increasing the Reynolds number Re, which is the ratio of the inertial to viscous forces [see Eq. (4)], can not only enhance such mixing, but also instigate various bifurcations to nonlinear oscillatory states [9]. The emergence of flow oscillations due to variations in Re suggests that different scenarios are possible along the route to chaos, whereby the system transitions from some ordered state to the neighborhood of a strange attractor [10].

The three most common routes to chaos are as follows:

(i) *Ruelle-Takens-Newhouse route*: Newhouse, Ruelle, and Takens [11] showed that a three-frequency quasi-periodic attractor generated through three successive Hopf bifurcations is inherently unstable to weak disturbances, with a tendency to break down into a chaotic attractor via a set of folding and stretching operations [12]. This route to chaos has been numerically identified in the flow through various wavy channels [13–15].

(ii) *Period-doubling route*: This route to chaos, discovered by Feigenbaum [16], features a cascade of period-doubling bifurcations, leading to self-similar structures in the bifurcation diagram. Although this route has been observed in thermoacoustic systems [17], circuits [18], and convective flows [19], it has yet to be reported for fluid flow in wavy channels.

(iii) *Intermittency route*: Pomeau and Manneville [20] discovered a route to chaos in which regular and chaotic dynamics alternate intermittently. Along this route, as the bifurcation parameter (e.g., Re) increases beyond a critical value, chaotic bursts appear increasingly prominently over a background of regular motion, eventually leading to a fully chaotic state. Three distinct types of intermittency were initially identified by Pomeau and Manneville [20]: (type-I) saddle-node bifurcation, (type-II) Hopf bifurcation, and (type-III) inverse period-doubling bifurcation. These were later joined by further types, such as crisis-induced intermittency and on-off intermittency [21]. In hydrodynamics (e.g., Rayleigh-Bénard convection), the intermittency route to chaos has been well studied as a possible pathway to turbulence [10]. For the flow through a wavy channel, Zhu *et al.* [15] observed temporal intermittency but not along the route to chaos. Therefore, whether the intermittency route to chaos

*mhd@connect.ust.hk
†larryli@ust.hk

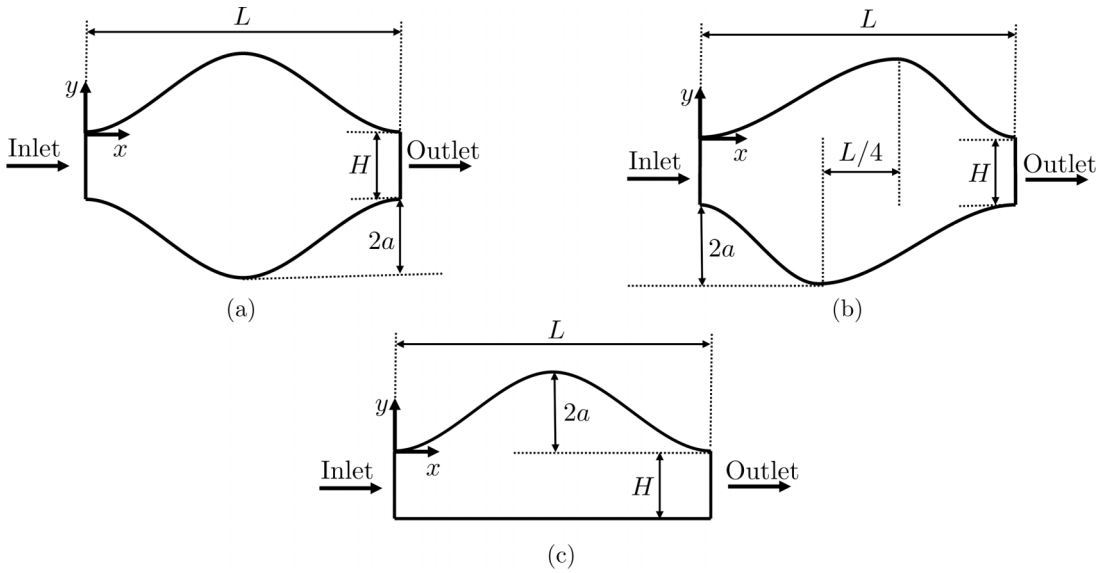

FIG. 1. Computational domain for the (a) symmetric, (b) asymmetric and (c) semiwavy channels used in this study. The geometrical parameters are $H/a = 12/7$ and $L/a = 8$ [9,25,26]. The flow is two-dimensional, incompressible, isothermal, and fully developed. The flow enters the channel from the left inlet and exits at the right outlet.

could exist in the flow through a wavy channel remains an open question.

II. PROBLEM DEFINITION

In this numerical study, we examine the bifurcations and routes to chaos in the two-dimensional flow through three canonical types of wavy channels: [Fig. 1(a)] a symmetric channel, [Fig. 1(b)] an asymmetric channel, and [Fig. 1(c)] a semi-wavy channel. For all three channels, the flow enters from the left inlet and exits at the right outlet. For the asymmetric channel [Fig. 1(b)], the top and bottom halves are offset in the streamwise direction by $L/4$, where L is the channel length. We consider incompressible, isothermal, fully developed wavy-channel flow [22] susceptible to both centrifugal instabilities [23] and shear (Kelvin-Helmholtz) instabilities [24]. Here, to permit both types of instabilities, we use the geometrical parameters from Nishimura *et al.* [25,26] and Harikrishnan *et al.* [9], namely $H/a = 12/7$ and $L/a = 8$, where H is the outlet height and a is the hump half-height, as defined in Fig. 1. These parameters are known to support both Kelvin-Helmholtz and centrifugal instabilities in wavy channel flow. Our bifurcation parameter is the Reynolds number, as defined in Eq. (4).

Our results show that all three classic routes to chaos can be found in this wavy-channel flow system. The symmetric channel experiences the period-doubling route, the semi-wavy channel experiences the intermittency route, and the asymmetric channel experiences both the intermittency and Ruelle-Takens-Newhouse routes. The intermittency observed here is found to conform to type-II of the Pomeau-Manneville scenario [20]. These findings provide researchers with new insights into how best to predict and manage chaotic flow oscillations in systems with wavy channels, such as micropower generation devices and the human heart. For example, massive fatty depositions in the atrium of the heart can cause chaotic blood flow, raising the risk of heartbeat disturbances and atrial arrhythmias [27]. This process can be viewed as a bifurcation, where changing the geometry of a wavy channel (atrium) can cause chaotic flow disturbances to emerge at a lower Re.

III. NUMERICAL METHODOLOGY

A. Governing equations

We consider two-dimensional, laminar, incompressible, isothermal, fully developed flow through a wavy channel, as shown in Fig. 1. The governing equations for this system are the mass and momentum equations [9,28]:

$$\nabla \cdot \mathbf{V} = 0 \tag{1}$$

$$\frac{\partial \mathbf{V}}{\partial t} + \mathbf{V} \cdot \nabla \mathbf{V} = -\frac{\nabla \tilde{p}}{\rho} + \nu \nabla^2 \mathbf{V} + \frac{\beta}{\rho}, \tag{2}$$

where $\mathbf{V}$, ρ, β, ν, and $\tilde{p}$ denote the velocity vector, fluid density, linear component of the pressure, kinematic viscosity and the reduced pressure. The values of β and $\tilde{p}$ are selected so as to satisfy cyclic boundary conditions at the inlet and outlet patches. The actual pressure can be written as [22]

$$p(x, y) = -\beta x + \tilde{p}(x, y). \tag{3}$$

As noted earlier, our bifurcation parameter is the Reynolds number, defined as

$$\mathrm{Re} \equiv \frac{u_0 H}{\nu}, \tag{4}$$

where u_0 is the spatially averaged velocity at the inlet, H is the height of the outlet (Fig. 1), and ν is the kinematic viscosity of the fluid. At the inlet and outlet patches, we impose cyclic boundary conditions such that $\eta\,(inlet) = \eta\,(outlet)$, where η can be $\mathbf{V}$ or $\tilde{p}$. The top and bottom patches are impermeable walls on which the no-slip condition is imposed. At $t = 0$, the flow in the computational domain is initialized with a velocity

corresponding to each value of Re. Previous studies [29–32] have shown that the use of a single wavy module with cyclic boundary conditions, rather than a long channel with several wavy modules, can reduce the computational cost while still enabling the flow instability mechanisms to be resolved. Further details on the cyclic boundary conditions used here can be found in Ref. [22].

B. Numerical simulations

We use OpenFOAM [33,34] to carry out direct numerical simulation of the flow in wavy channels at different Re. The PISO (pressure-implicit with splitting of operators) algorithm is used to solve the governing equations. The spatial and temporal derivatives are approximated via a second-order central differencing scheme and a second-order Euler backward differencing scheme, respectively. For the mass and momentum equations, the convergence criteria are set to 10^{-6}. In all the simulations, the maximum value of the Courant number is kept at or below 0.3. A grid independence check and validation of our numerical framework can be found in Appendices A and B.

C. Nonlinear time-series analysis

For the symmetric and semiwavy channels, we extract time traces of the instantaneous flow velocity at the location $(L/2, a)$. For the asymmetric channel, we use a velocity probe location of $(5L/8, a)$. To generate bifurcation diagrams, we plot the local peaks of the transverse velocity component (v) versus Re. We also use the velocity time traces to reconstruct the phase space via the embedding theorem of Takens [35]. We use the average mutual information [36] and the algorithm of Cao [37] to find the optimal values of the embedding delay time (τ) and the embedding dimension (m), respectively. We plot the phase portrait and Poincaré map to identify the topology of the attractors present in the system [38,39]. Using the algorithm of Grassberger and Procaccia [40], we compute the correlation dimension as a quantitative measure of the number of active degrees of freedom. We plot the correlation sum ($C(m, R)$) and its local slope ($D_c = \partial \log C(m, R)/\partial \log R$) as a function of the normalized Euclidean distance, $R/R_{\max}$, for different values of m. The value of D_c should be zero, one, two and a noninteger for, respectively, a fixed point (steady flow), a limit cycle (periodic motion), a two-frequency quasi-periodic torus, and a strange attractor [41]. Under certain conditions, we observe intermittency, whose type we identify by analyzing the Poincaré map, the recurrence plot, the probability distribution of the interchaos time, and the variation of the average interchaos time versus a normalized bifurcation parameter [42,43].

IV. RESULTS AND DISCUSSION

A. Symmetric wavy channel

An overview of the temporal dynamics of the flow in the symmetric wavy channel is shown in Fig. 2. The bifurcation diagram [Fig. 2(a)] reveals the existence of four different dynamical states as Re increases: a fixed point (steady flow) → a period-1 limit cycle → T^2 quasi-periodicity → a period-2 limit cycle → a period-4 limit cycle → chaos. This constitutes direct evidence of the period-doubling route to chaos [16]. These dynamical states are examined further below:

(i) *A fixed point (steady flow)*: For $\mathrm{Re} < 160$ (brown markers/lines), viscous damping is sufficient to overcome the destabilizing influence of shear (Kelvin-Helmholtz) and centrifugal forces. As a result, the flow is steady with no large-scale self-excited oscillations.

(ii) *Quasiperiodicity between period-k limit cycles*: The window of T^2 quasiperiodicity ($200 \leqslant \mathrm{Re} < 500$, orange) is sandwiched by three different types of limit cycles: period-1 ($160 \leqslant \mathrm{Re} < 200$, black), period-2 ($500 \leqslant \mathrm{Re} < 560$, green), and period-4 ($560 \leqslant \mathrm{Re} < 680$, purple). To examine the period-2^k limit cycles and the T^2 quasiperiodic state, we choose representative cases of $\mathrm{Re} = 190$ for period-1, $\mathrm{Re} = 450$ for quasiperiodic, $\mathrm{Re} = 530$ for period-2, and $\mathrm{Re} = 610$ for period-4 states. On increasing Re to around 160, we find that the system becomes self-excited, transitioning from a fixed point (steady flow) to a period-1 limit cycle with a dominant frequency of $f_1 \simeq 0.053$ Hz via a Hopf bifurcation. At $\mathrm{Re} = 190$, the existence of a period-1 state is supported by the time series exhibiting a single peak within each oscillation cycle [Fig. 2(b)], a closed orbit in the phase portrait [Fig. 2(c)], and a single intercept in the one-sided Poincaré map [Fig. 2(d)]. As Re approaches 200, the flow begins to oscillate at two incommensurate frequencies, $f_2 \simeq 0.106$ Hz and $f_3 \simeq 0.230$ Hz, where f_3/f_2 is not a rational number (for brevity, the spectra are not shown), confirming the existence of a T^2 quasiperiodic state. This assessment is substantiated by the aperiodic time trace at $\mathrm{Re} = 450$ [Fig. 2(g)], along with an ergodic torus and a closed ring, respectively, in the phase portrait [Fig. 2(h)] and the one-sided Poincaré map [Fig. 2(i)]. On increasing Re to around 500, we find that the two incommensurate frequencies, f_2 and f_3, shift to commensurate values, $f_4 \simeq 0.130$ Hz, and $f_5 \simeq 2f_4 \simeq 0.260$ Hz, indicating a frequency-locking condition that produces a period-2 limit cycle [44]. This is clear from the time series at $\mathrm{Re} = 530$ [Fig. 2(l)], which shows two peaks within each oscillation cycle. The result is a double-loop structure in the phase portrait [Fig. 2(m)] and two discrete intercepts in the one-sided Poincaré map [Fig. 2(n)]. Increasing Re further to around 560 results in the emergence of four commensurate frequencies that are locked into one another, $f_6 \simeq 0.075$ Hz, $f_7 = 2f_6 \simeq 0.150$ Hz, $f_8 = 3f_6 \simeq 0.225$ Hz, $f_9 = 4f_6 \simeq 0.300$ Hz, confirming the existence of a period-4 limit cycle. This observation is supported by the time trace at $\mathrm{Re} = 610$ [Fig. 2(q)], which shows four peaks within each oscillation cycle. This produces a quadruple-loop structure in the phase portrait [Fig. 2(r)] and four intercepts in the one-sided Poincaré map [Fig. 2(s)]. As for the correlation dimension, we find that for $\mathrm{Re} = 190$ [Figs. 2(e) and 2(f)], $\mathrm{Re} = 530$ [Figs. 2(o) and 2(p)], and $\mathrm{Re} = 610$ [Figs. 2 (t) and 2(u)], $D_c \simeq 1$ over $10^{-3} < R/R_{\max} < 10^{-1}$ (self-similar scaling range) with $m = 6$, confirming the presence of a limit-cycle attractor. For $\mathrm{Re} = 450$ [Figs. 2(j) and 2(k)], we find $D_c \simeq 2$ over $10^{-2} < R/R_{\max} < 10^{-1}$ with $m = 13$, confirming the existence of a T^2 quasi-periodic attractor with two incommensurate modes.

(iii) *Chaos*: When $\mathrm{Re} \geqslant 680$ (blue), the flow becomes chaotic, causing the data points in the bifurcation diagram to become more scattered [Fig. 2(a)]. The time series of v at

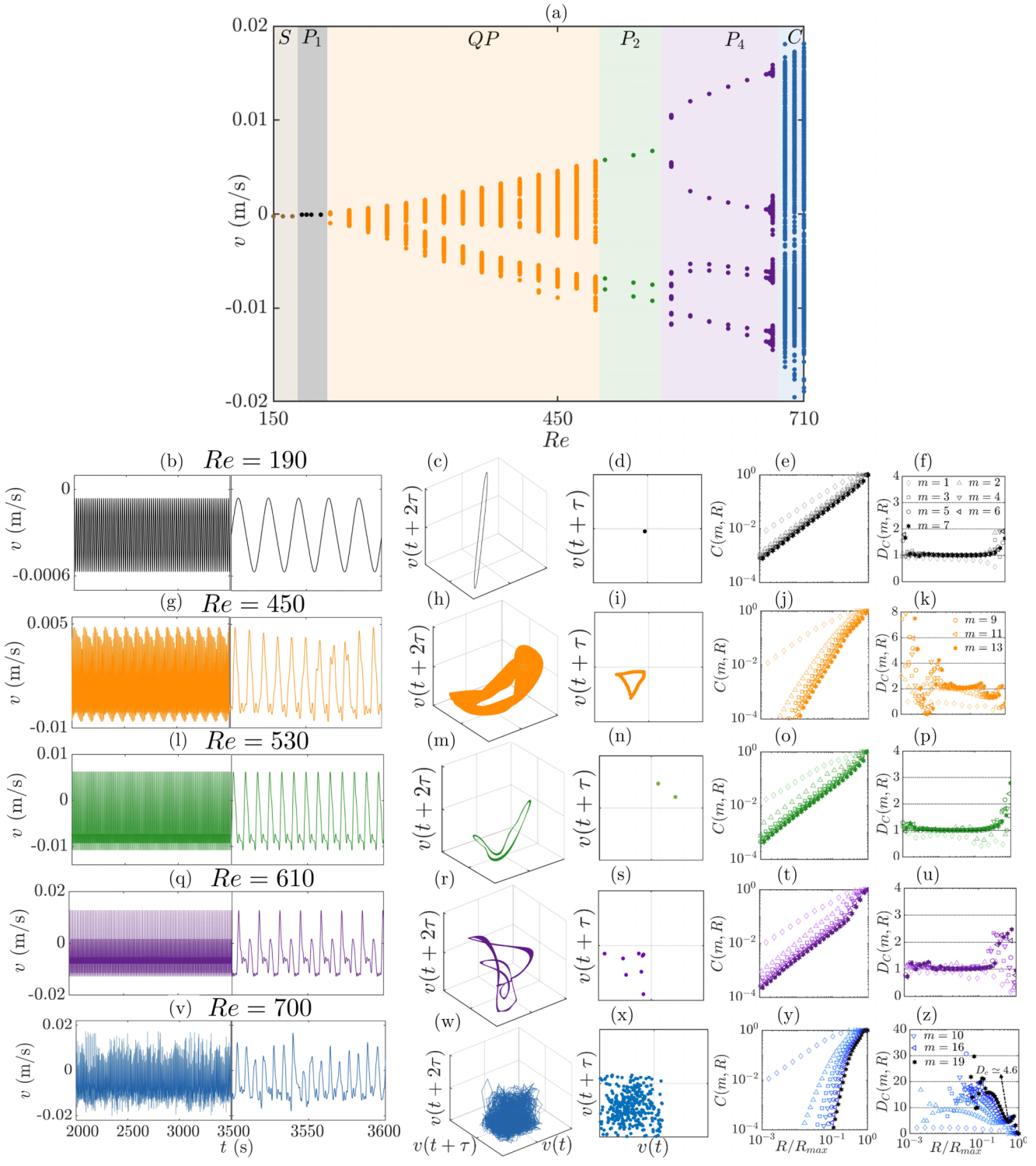

FIG. 2. Period-doubling route to chaos in the flow through a symmetric wavy channel. The bifurcation diagram is shown in panel (a). Five different states are highlighted: (b)–(f), black, a period-1 limit cycle, (g)–(k), yellow, T^2 quasiperiodicity, (l)–(p), green, a period-2 limit cycle, (q)–(u), purple, a period-4 limit cycle, and (v)–(z), blue, low-dimensional chaos. Skipping (a), the columns show, from left to right, the time series of v, the phase portrait, the one-sided Poincaré map, the correlation sum, and the slope of the correlation sum.

Re = 700 [Fig. 2(v)] is highly irregular, giving rise to complex fractal structures in phase space [Figs. 2(w) and 2(x)]. The plot of $C(m, R)$ [Fig. 2(y)] and D_c [Fig. 2(z)] reveal a non-integer value of $D_c \simeq 4.6$ over the self-similar scaling range ($0.3 < R/R_{\max} < 0.6$) with $m = 19$, confirming the presence of a strange attractor [21]. Such a low value of D_c reveals that the chaotic dynamics are low-dimensional [21].

In summary, we have presented evidence of a bifurcation cascade arising from the period-doubling route to chaos as Re increases. The presence of a T^2 quasi-periodic window

between the period-1 and period-2 windows is believed to arise from the emergence of an incommensurate mode following the period-1 state. This mode then undergoes frequency-locking as Re increases, eventually taking on a commensurate frequency. Resolving higher-order period-2^k (e.g., period-8) states is challenging [Fig. 2(a)] because the Re range in which such states exist becomes increasingly narrow.

B. Asymmetric wavy channel

An overview of the temporal dynamics of the flow in the asymmetric wavy channel is shown in Fig. 3. On increasing Re [Fig. 3(a)], we first find evidence of the Ruelle-Takens-Newhouse route to chaos [11]: a fixed point (steady flow) → a period-1 limit cycle → T^2 quasi-periodicity → chaos. With further increases in Re [Fig. 3(a)], we find evidence of the intermittency route to chaos [20]: intermittency → chaos → period-k limit cycles → chaos. Below we examine these states in turn:

(i) *A fixed point (steady flow)*: For Re $<$ 180 (brown), the flow is stabilized by the effects of viscosity, resulting in a nominally time-independent state. Compared with the symmetric channel, the asymmetric channel is found to be more resistant to flow instabilities, remaining dynamically stable at higher values of Re.

(ii) *Period-k limit cycles*: The bifurcation diagram [Fig. 3(a)] contains two different limit-cycle windows, as denoted by black markers/lines. In the first window ($180 \leqslant Re < 200$), the flow is self-excited in a period-1 limit cycle. The time series of v at Re = 190 [Fig. 3(b)] is periodic with a dominant frequency of $f_1 = 0.053$ Hz. There is a closed orbit in the phase portrait [Fig. 3(c)] and a single intercept in the Poincaré map [Fig. 3(d)], confirming the existence of a period-1 limit cycle. Figures 3(e) and 3(f) show that $D_c \simeq 1$ over $10^{-3} < R/R_{\max} < 10^{-1}$, further corroborating the existence of a limit cycle. In the second window ($520 \leqslant Re < 560$), we find period-3, period-4 and period-5 limit cycles. The time series of v at Re = 550, as a prototypical case of a period-5 limit cycle, produces a quintuple-loop structure in the phase portrait [Fig. 3(u)] and five intercepts in the one-sided Poincaré map [Fig. 3(v)]. This limit-cycle behavior is also verified by Figs. 3(w) and 3(x), which show $D_c \simeq 1$ over $8 \times 10^{-3} < R/R_{\max} < 6 \times 10^{-2}$.

(iii) *Quasi-periodicity*: At slightly higher Reynolds numbers ($200 \leqslant Re < 420$, orange), two new incommensurate frequencies emerge, $f_2 = 0.091$ Hz and $f_3 = 0.336$ Hz, leading to a T^2 quasiperiodic state. This concurs with the aperiodic nature of the time series at Re = 350 [Fig. 3(g)], which produces an ergodic torus in the phase portrait [Fig. 3(h)] and a closed ring in the one-sided Poincaré map [Fig. 3(i)]. From Figs. 3(j) and 3(k), we note that $D_c \simeq 2$ over $0.07 < R/R_{\max} < 0.25$, confirming the presence of T^2 quasiperiodicity.

(iv) *Chaos*: In the bifurcation diagram [Fig. 3(a)], we find three separate windows of chaos ($420 \leqslant Re < 475$, $505 \leqslant Re < 520$, $560 \leqslant Re < 600$) in which the data points are scattered. The time series of v at Re = 450 is highly irregular, producing complex fractal structures in phase space [Fig. 3(m) and 3(n)]. Figures 3(o) and 3(p) reveal that $D_c \simeq 3.2$ (a noninteger) over $0.05 < R/R_{\max} < 0.16$, confirming the existence of a strange attractor with low-dimensional chaotic dynamics [21].

(v) *Intermittency*: At $475 \leqslant Re < 505$ (red), the flow exhibits intermittency by alternating between chaotic and periodic epochs. This can be seen directly in the time series of v at Re = 490 [Fig. 3(q)], where high-amplitude chaotic bursts appear intermittently over mid-amplitude periodic epochs. The phase portrait [Fig. 3(r)] and Poincaré map [Fig. 3(s)] also reveal that the system switches between a limit-cycle attractor (an inner closed loop) and a strange attractor (outer orbit). If the phase trajectory is initially near the limit-cycle attractor, it stays there for a while, then bursts out to the strange attractor, but is reinjected later. As Re increases, the chaotic epochs lengthen in time, eventually causing the flow dynamics to be dominated by sustained chaos.

Next, we identify the specific type of intermittency present in the asymmetric channel. We show in Fig. 4(a) the time series of v at Re = 490 to illustrate chaotic bursts appearing over a background of periodic epochs. We also show the probability distribution P of the duration of the periodic epochs [i.e., the interchaos time, t_P; Fig. 4(b)], the recurrence plot [Fig. 4(c)], the power spectral density (PSD) of the v time series [Fig. 4(d)], the Poincaré section [Fig. 4(e)], and the average inter-chaos time versus the normalized Re [Fig. 4(f)]. Figure 4(a) shows that the high-amplitude chaotic bursts are interspersed among mid-amplitude periodic epochs. The PSD [Fig. 4(d)] features a set of broadband components during the chaotic bursts, but only two sharp peaks during the periodic epochs (at f_1, f_2, and $f_2 \simeq 2f_1$). These observations reinforce the view that this is a state of intermittency involving temporal switching between periodic and chaotic epochs.

We determine the intermittency to be type-II of the Pomeau-Manneville scenario [20]. This is based on four pieces of evidence: (i) P decays according to a power law with an exponent close to -2, which is estimated via nonlinear least-squares regression [Fig. 4(b)] [45–49], (ii) the recurrence plot shows kitelike structures [Fig. 4(c)] [50–52], (iii) the Poincaré section shows spiraling trajectories [Fig. 4(e)] [53–55], and (iv) the average interchaos time is inversely proportional to the normalized bifurcation parameter, $< t_P > \sim [(\mathrm{Re} - \mathrm{Re}_0)/\mathrm{Re}_0]^{-1}$ [Fig. 4(f)] [47,53–56]; here $\mathrm{Re}_0 = 475$ corresponds to the onset of intermittency.

In summary, we have shown that both the Ruelle-Takens-Newhouse and intermittency routes to chaos can arise in the flow through an asymmetric wavy channel. We identified the intermittency as belonging to type-II of the Pomeau-Manneville scenario [20]. We found that introducing asymmetry in a wavy channel can enrich the complexity of the flow dynamics, allowing for different routes to chaos. Regarding real-world implications, it is known that massive fatty deposition in the atrium can trigger disturbances and atrial arrhythmias [27]. Our findings suggest that this may occur because the deposition of fat in the atrium makes its geometry more asymmetric, inducing chaotic flow at lower Re.

C. Semiwavy channel

Moving on to the semiwavy channel [Fig. 5], we see from the bifurcation diagram [Fig. 5(a)] that there are four

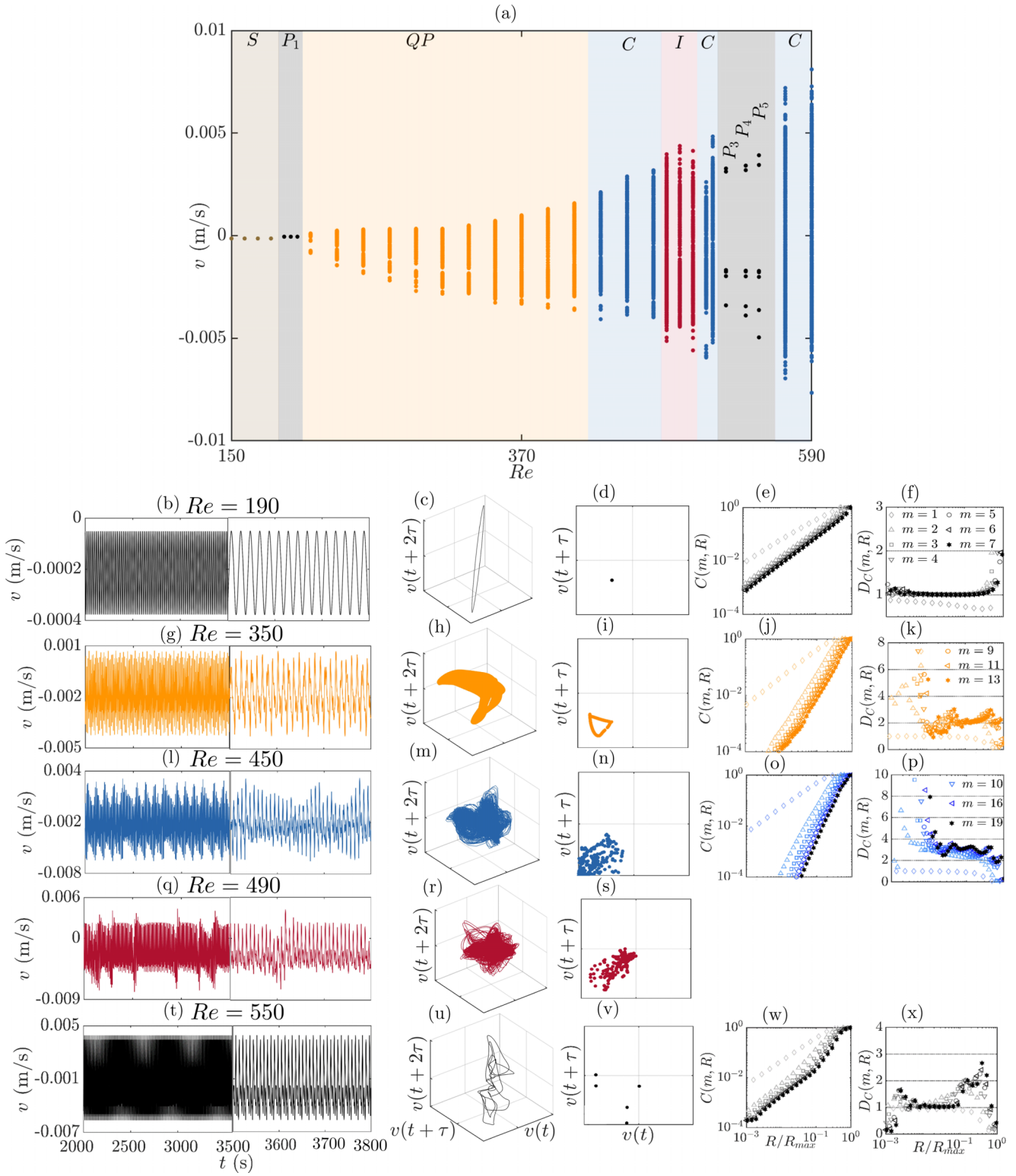

FIG. 3. Ruelle-Takens-Newhouse and intermittency routes to chaos in the flow through an asymmetric wavy channel. The bifurcation diagram is shown in (a). Five different states are highlighted: (b)–(f) black, a period-1 limit cycle, (g)–(k), yellow, T^2 quasiperiodicity, (l)–(p), blue, low-dimensional chaos, (q)–(s), red intermittency, and (t)–(x), black, a period-5 limit cycle. Skipping (a), the columns show, from left to right, the time series of v, the phase portrait, the one-sided Poincaré map, the correlation sum, and the slope of the correlation sum.

dynamical states: a fixed point (steady state) → a period-1 limit cycle → intermittency → chaos. As before, this indicates the presence of the intermittency route to chaos. We examine each state in turn.

(i) *A fixed point (steady flow)*: For Re < 280 (brown), the flow is still dominated by viscous effects, with no sign of self-excited oscillations. We find that flow in the semiwavy channel remains steady for higher Re values than those in the

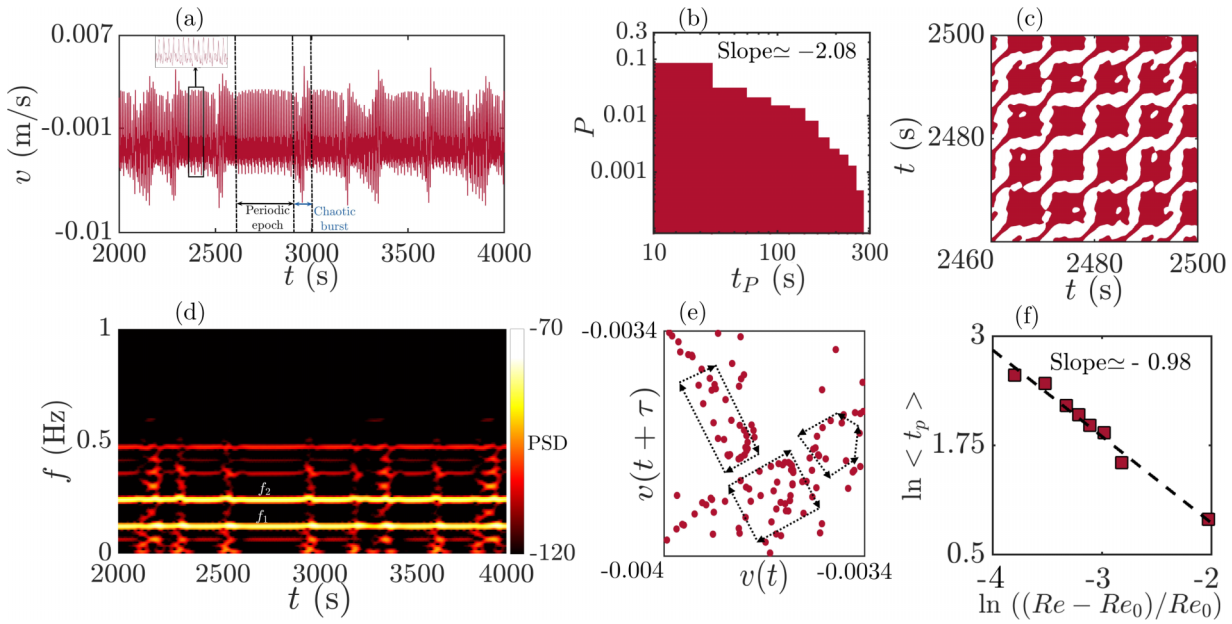

FIG. 4. Type-II intermittency in the flow through an asymmetric wavy channel at Re = 490: (a) the time trace of v showing chaotic bursts amidst a periodic background, (b) the probability distribution of the interchaos time, (c) the recurrence plot featuring kitelike structures, (d) the PSD where the periodic epochs are dominated by narrowband components at f_1 and f_2 ($f_2 \simeq 2f_1$) and the chaotic bursts are dominated by broader peaks, (e) the Poincaré section featuring spiraling patterns, and (f) the average interchaos time versus the normalized bifurcation parameter.

symmetric and asymmetric channels of the previous sections. This is attributed to the weaker adverse and favorable pressure gradients arising from the flat bottom surface of the semiwavy channel.

(ii) *Period-1 limit cycle*: An increase in the Reynolds number ($280 \leqslant \mathrm{Re} < 845$, black) causes the flow to become self-excited, transitioning to a period-1 limit cycle at a dominant frequency of $f \simeq 0.520$ Hz. The regularity of the v time trace at Re = 600 [Fig. 5(b)] supports this view, as does the closed orbit in the phase portrait [Fig. 5(c)] and the single intercept in the one-sided Poincaré map [Fig. 5(d)]. Figures 5(e) and 5(f) show that $D_c \simeq 1$ over $10^{-3} < R/R_{\max} < 0.6$, confirming the presence of periodicity. The periodicity is relatively robust, covering a wider Re window than for the cases of the symmetric and asymmetric channels.

(iii) *Intermittency*: For $845 \leqslant \mathrm{Re} < 885$ (red), the data points in the bifurcation diagram become more scattered, with the time trace at Re = 860 [Fig. 5(g)] exhibiting high-amplitude chaotic bursts amidst a background of low-amplitude periodic epochs. This is the classic sign of intermittency. The phase portrait [Fig. 5(h)] and the one-sided Poincaré map [Fig. 5(i)] show that at the onset of intermittency (i.e., the first sign of chaotic bursts), the phase trajectory moves away from the vicinity of the inner periodic orbit and towards several irregular outer orbits belonging to a strange attractor. Once a chaotic burst ends, however, the phase trajectory is reinjected to the neighborhood of the periodic orbit (inner loops). As Re increases, the chaotic bursts appear more frequently and with a longer duration, until they dominate the flow motion at the upper Re limit of the intermittency window. A detailed analysis of the intermittency characteristics, similar to that conducted for the asymmetric channel [Fig. 4], will be presented in Fig. 6.

(iv) *Chaos*: For $\mathrm{Re} \geqslant 885$ (blue), the data points in the bifurcation diagram become even more scattered. The v time series at Re = 960 [Fig. 5(j)] produces complex fractal structures in phase space [Figs. 5(k) and 5(l)]. Figures 5(m) and 5(n) show that $D_c \simeq 4.4$ (a noninteger) over $0.07 < R/R_{\max} < 0.1$, confirming the presence of a strange attractor.

Next, we identify the specific type of intermittency present in the semiwavy channel. Figure 6(a) shows the time trace of v at Re = 860, where high-amplitude chaotic bursts can be seen appearing intermittently over a background of low-amplitude periodic epochs. Figure 6(b) shows that P decays according to a power law with an exponent close to -2, indicating the presence of type-II intermittency [45–49]. The recurrence plot is seen to contain kite-like structures [Fig. 6(c)], providing further evidence of type-II intermittency [50–52]. The PSD reveals that the chaotic bursts contain a broad range of frequencies, while the periodic epochs are dominated by three sharp peaks at commensurate frequencies [Fig. 6(d)]: $f_2 \approx 2f_1 \simeq 0.474$ Hz, and $f_3 \approx 3f_1 \simeq 0.711$ Hz. Further evidence of type-II intermittency can be found in the spiraling patterns of the Poincaré section [Fig. 6(e)] [53–55]. Finally, an examination of the average interchaos time [Fig. 6(f)] reveals that it is inversely proportional to the normalized bifurcation parameter, $< t_P > \sim [(\mathrm{Re} - \mathrm{Re}_0)/\mathrm{Re}_0]^{-1}$, further substantiating the presence of type-II intermittency [47,53–56]. Here, $\mathrm{Re}_0 = 845$ is the Reynolds number at the start of the intermittency window.

In summary, we have shown that the flow through a semiwavy channel can transition to chaos via the intermittency route. The intermittency is determined as conforming to type-II of the Pomeau-Manneville scenario [20]. Compared with the symmetric and asymmetric channels, the

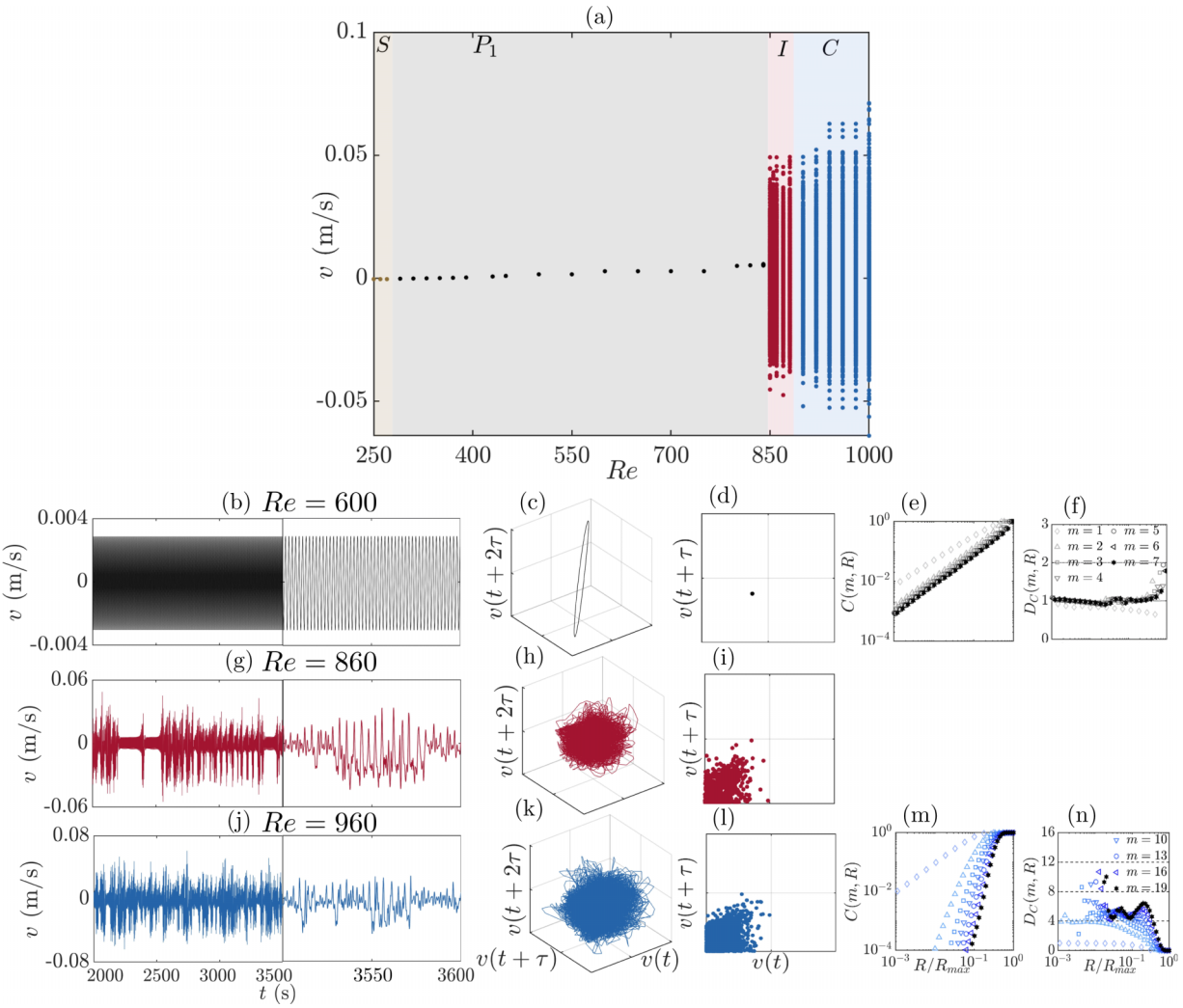

FIG. 5. Intermittency route to chaos in the flow through a semi-wavy channel. The bifurcation diagram is shown in panel (a). Three different states are highlighted: (b)–(f), black, a period-1 limit cycle, (g)–(i), red, intermittency, and (j)–(n), blue, low-dimensional chaos. Skipping (a), the columns show, from left to right, the time series of v, the phase portrait, the one-sided Poincaré map, the correlation sum, and the slope of the correlation sum.

semiwavy channel is found to have a wider window of period-1 dynamics, implying that it is more difficult to activate additional degrees of freedom in this specific geometry.

As a final remark, we observe unstable invariant sets for the semiwavy channel. In the vicinity of an unstable invariant set, the phase trajectory is attracted towards it in some directions, but is repelled in other directions [57]. Identifying the existence of unstable invariant sets is important because it could help researchers understand, predict and control the pathways and mechanisms governing the evolution of a nonlinear dynamical system from one state to another [58]. The role of unstable invariant sets is well known in the hydrodynamics community, especially in the context of turbulence transition in pipe flow [59], but we believe that they have not, until now, been observed in wavy-channel flow.

Figure 7 shows the temporal dynamics of the flow through the semiwavy channel at Re = 835 and 840. For both values of Re, the system is first attracted to a quasiperiodic attractor (orange) but is then repelled to a high-amplitude state associated with a chaotic saddle (blue). The system remains near this unstable invariant set for a short period, before eventually settling on a period-1 limit-cycle attractor (black). The observation that the unstable chaotic state exhibits higher amplitude bursts at higher Re is consistent with the data in Fig. 5.

D. Flow pattern and friction factor

Figure 8 shows the instantaneous and time-averaged streamlines and contours of the dimensionless streamwise velocity for all three channels at different Re, along with their corresponding dynamical state and friction factor (f). The blue, green, and red regions indicate reversed flow ($u/u_0 < 0$), decelerated flow ($0 < u/u_0 < 1$), and accelerated flow ($u/u_0 > 1$), respectively.

For the symmetric channel (top two rows of Fig. 8), at Re = 190, only minor differences arise between the instantaneous and time-averaged flow patterns owing to the low Re. The instantaneous contours of the accelerated flow (central jet

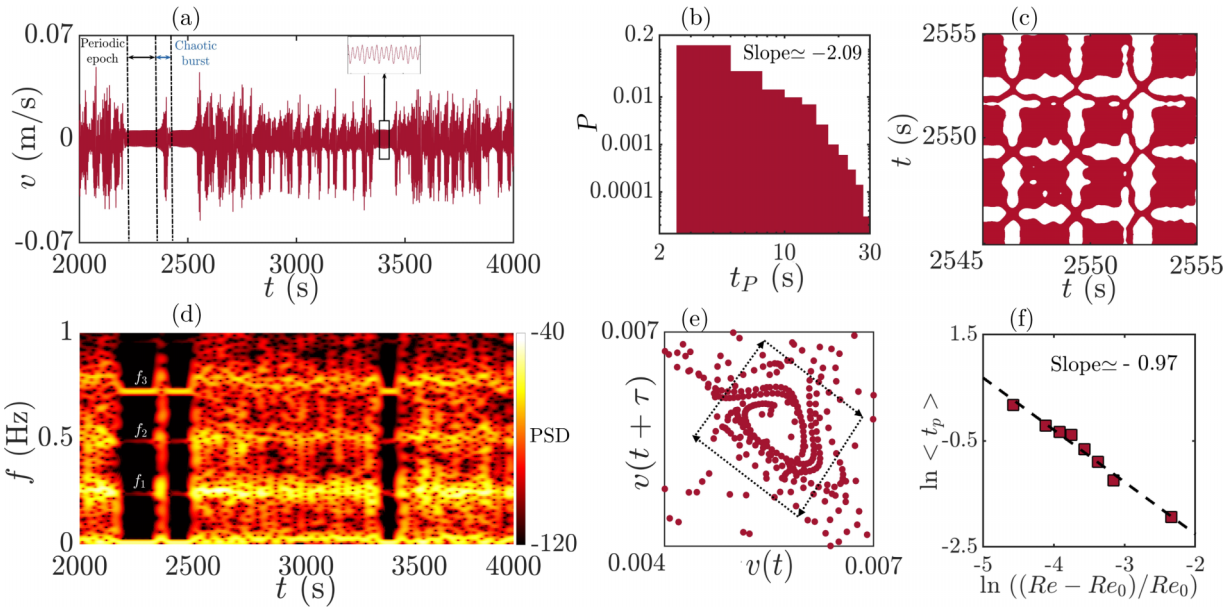

FIG. 6. Type-II intermittency in the flow through a semiwavy channel at Re = 860: (a) the time trace of v showing chaotic bursts amidst a periodic background, (b) the probability distribution of the interchaos time, (c) the recurrence plot featuring kitelike structures, (d) the PSD where the periodic epochs are dominated by narrowband components at f_1, f_2 and f_3 ($f_2 \simeq 2f_1$ and $f_3 \simeq 3f_1$) and the chaotic bursts are dominated by broader peaks, (e) the Poincaré map featuring spiraling patterns, and (f) the average interchaos time versus the normalized bifurcation parameter.

in red) exhibit an undulating pattern, with a significant extent of reversed flow (blue regions) relative to higher Re, which increases the flow resistance and thus f. Two large vortices appear, one in the top groove and the other in the bottom groove. When Re = 450 (quasiperiodicity), the instantaneous contours of the accelerated flow show higher amplitudes, consistent with the time series shown in Fig. 2(g). The reduction in f for Re > 190 is due to a smaller reversed flow region, a delay in flow separation, and earlier reattachment. This observation is consistent with the findings of Nishimura *et al.* [25], where for Re > 230, f experiences only minor variations. Meanwhile, the time-averaged contours show that the structure of the two large vortices in the grooves is maintained. However, for Re > 450, two small vortices appear in the top and bottom grooves. At Re = 530 (period-2 limit cycle), the accelerated flow (central jet) in the instantaneous contours exhibits more pronounced undulations, but the structure of the two main vortices is still recognizable. At Re = 610 (period-4 limit cycle), the upper vortex is distorted and the central jet exhibits even more marked undulations, indicating more irregular dynamics at higher Re. At Re = 700 (chaos), the central jet becomes highly distorted and the two main

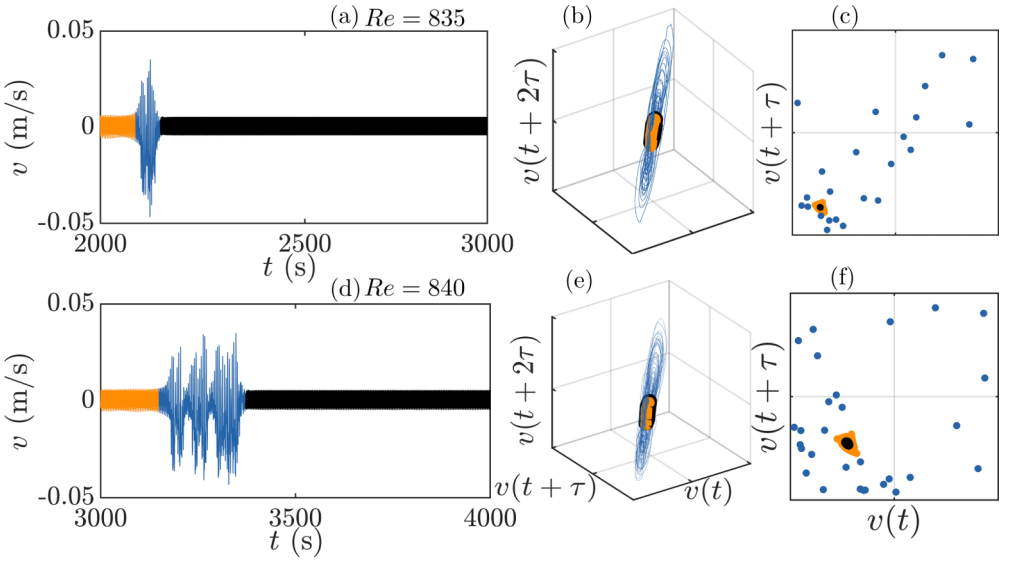

FIG. 7. Evidence of an unstable invariant set (chaotic saddle) in the flow through a semiwavy channel at two different Re values: (a)–(c) Re = 835 and (d)–(f) Re = 840. From left to right, they show the time trace of v, the phase portrait, and the Poincaré map.

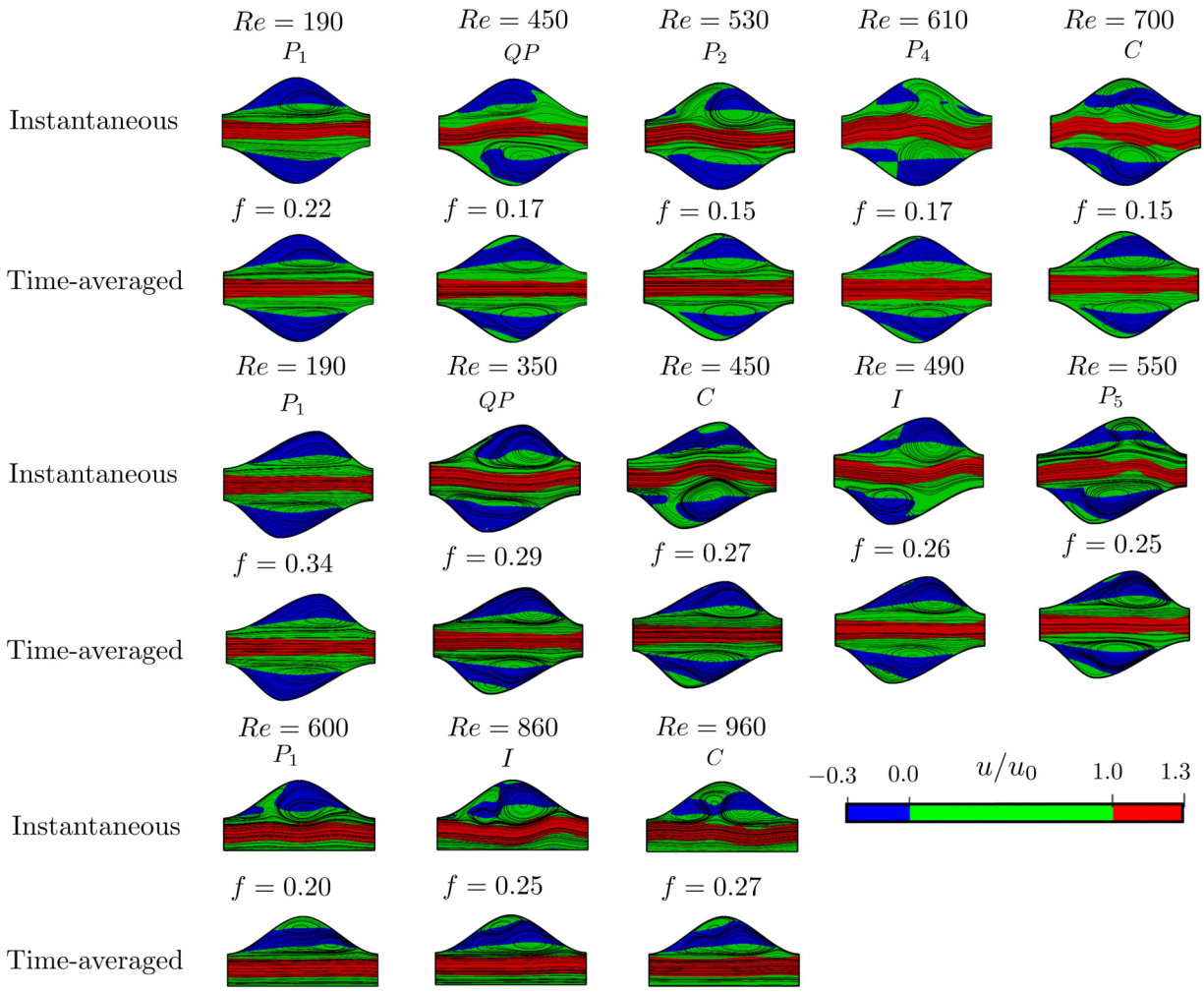

FIG. 8. Instantaneous and time-averaged streamlines and streamwise velocity contours for the three channel geometries. The blue, green, and red regions denote reversed flow ($u/u_0 < 0$), decelerated flow ($0 < u/u_0 < 1$), and accelerated flow ($u/u_0 > 1$), respectively. P_k, period-k limit cycle; QP, quasiperiodicity; C, chaos; I, intermittency.

vortices are destroyed, consistent with the presence of a strange attractor.

For the asymmetric channel (middle two rows of Fig. 8), higher shear stresses lead to higher f at all Re relative to the symmetric channel. Simulation data shown in Appendix A support this observation, as the velocity profile is symmetric for the symmetric channel [see Fig. 9(a)] but asymmetric for the asymmetric channel [see Fig. 9(b)]. The asymmetry in the velocity profile causes a stronger velocity gradient and hence a higher f. At Re = 190 (period-1 limit cycle), the instantaneous and time-averaged contours appear similar, with two large vortices present in the top and bottom grooves. For Re > 190, f decreases to a relatively constant value, similar to the case of the symmetric channel. At Re = 350 (quasi-periodicity), the central jet and the two main vortices become distorted, while for Re > 350, a small (third) vortex emerges in the bottom groove. At Re = 450 (chaos), the instantaneous contours reveal that the central jet and the vortices are modified such that different vortices are dispersed within the grooves. At Re = 490 (intermittency), the instantaneous contours show a moderate level of distortion of the main vortices and the central jet. At Re = 550 (period-5 limit cycle), the upper vortex and the central jet are highly disrupted, consistent with the emergence of chaos at higher Re [see Fig. 3(a)].

For the semiwavy channel (bottom two rows of Fig. 8), contrary to the other two channels, f increases with increasing Re owing to the flat bottom surface, which promotes boundary layer development and enhances momentum diffusion. At Re = 600 (period-1 limit cycle), the instantaneous contours reveal that the central jet is largely straight, with the single groove hosting a large vortex. However, in the time-averaged contours, this main vortex appears as two vortices next to each other. At Re = 860 (intermittency), the instantaneous contours show a moderate level of distortion of both the main vortex and the central jet, indicating more irregularity at higher Re. Finally, at Re = 960 (chaos), the central jet and the main vortex become highly distorted, consistent with the dominance of chaos.

It is worth noting that the study of fluid flow in two dimensions serves as a simplified yet valuable approach to understanding the fundamental flow physics. By focusing on two-dimensional simulations, we can isolate complex flow phenomena in a more controlled setting, which would be more

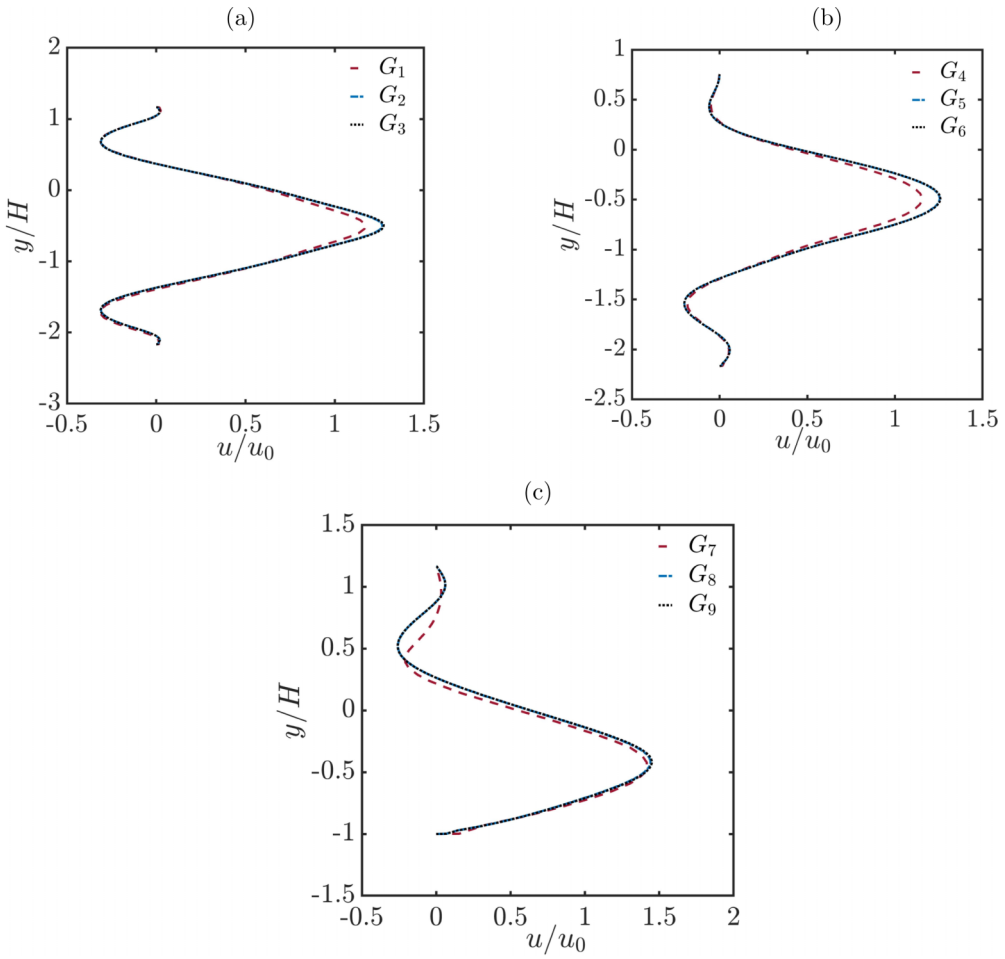

FIG. 9. Grid independence check using the dimensionless streamwise velocity profile u/u_0 for the (a) symmetric, (b) asymmetric, and (c) semiwavy channels.

computationally expensive and difficult to interpret than if it were done in three dimensions.

It is also important to recognize the limitations of two-dimensional simulations. Real-world flows are inherently three dimensional, and many flow phenomena—such as turbulence, vortex dynamics and secondary flows—can only be fully captured in three-dimensional simulations.

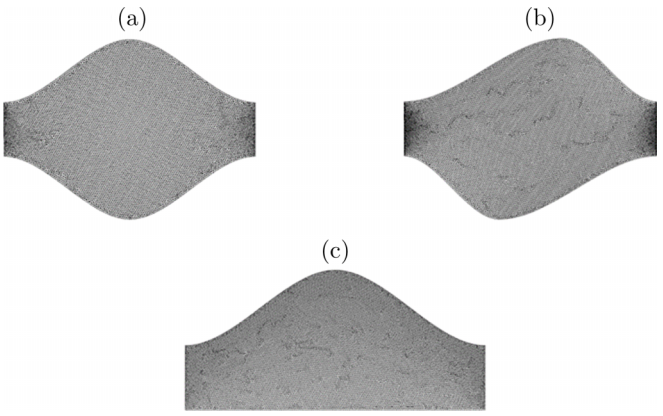

FIG. 10. Computational domain for the (a) symmetric, (b) asymmetric, and (c) semiwavy channels.

Therefore, while two-dimensional simulations can provide valuable insights into the underlying physics and can guide the development of theoretical models, they should always be supplemented with three-dimensional simulations in order to gain a complete representation of the real-world flow behavior [60]. Nevertheless, the two-dimensional assumption remains valid at low Re for two-dimensional geometries in which the flow is laminar or at the onset of transition, such as the flow over a cylinder at $\mathrm{Re} \leqslant 200$ [61,62] or the flow through a two-dimensional channel at $\mathrm{Re} \leqslant 1000$ [63,64]. Thus, the two-dimensional assumption should be valid in this study as the Re values used are relatively low ($\mathrm{Re} \leqslant 1000$).

As for the relation between two- and three-dimensional simulations, it is generally accepted that two-dimensional simulations can provide qualitatively similar flow patterns to three-dimensional simulations for laminar and transitional flows. However, quantitative differences can be significant for fully turbulent flows. The absence of streamwise vortices and three-dimensional coherent structures in two-dimensional flow tends to lower the Re value at which the transition from laminar to turbulent flow occurs [65]. Therefore, we do not expect the two-dimensional assumption to affect our conclusions, but it may have reduced the Re value at which transition occurs.

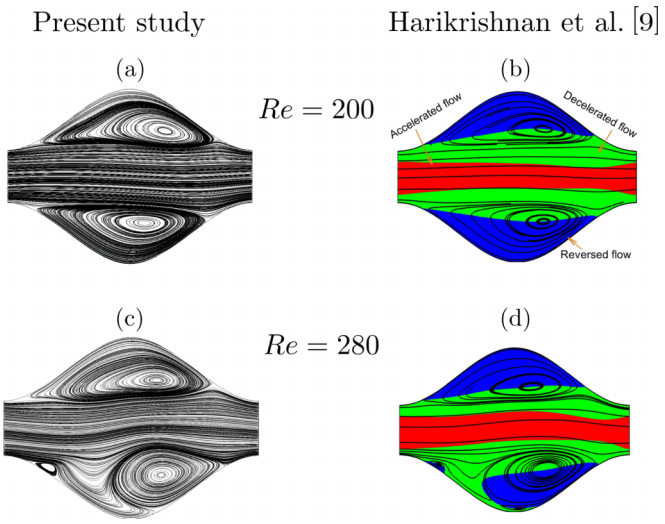

FIG. 11. Validation of our numerical framework via streamlines: (a), (c) our simulations and (b), (d) those by Harikrishnan *et al.* [9].

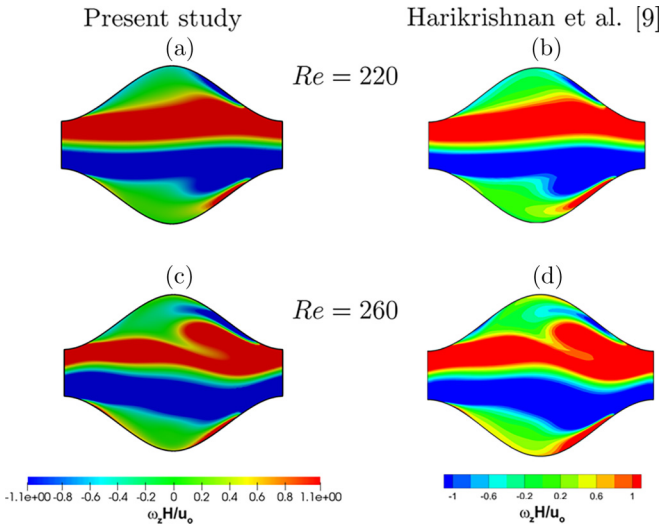

FIG. 12. Validation of our numerical framework via nondimensional z-vorticity contours: (a), (c) our simulations and (b), (d) those by Harikrishnan *et al.* [9].

V. CONCLUSIONS

In this study, we have numerically investigated the two-dimensional, laminar, incompressible, isothermal flow through a wavy channel, with a focus on the effects of channel geometry on the nonlinear dynamics and routes to chaos. Using an array of tools from dynamical systems theory, we found the period-doubling route to chaos in a symmetric channel, the Ruelle-Takens-Newhouse route in an asymmetric channel, and the intermittency route in both asymmetric and semiwavy channels. Regardless of the channel geometry, we determined that the intermittency present in the system conforms to type-II of the Pomeau-Manneville scenario. For the semiwavy channel, we showed that the flow can transition from an initial quasiperiodic state to a final period-1 limit-cycle state via an unstable invariant set (chaotic saddle). These results show that breaking the symmetry of a wavy channel cannot only change the critical Reynolds number required for chaos, but also introduce new bifurcations en route to chaos itself. This study could open up new directions for the prediction and management of chaotic flow oscillations in various biological and technological systems containing wavy channels, such as micro-combustors and the human heart.

ACKNOWLEDGMENTS

This work was supported by the Research Grants Council of Hong Kong (Projects No. 16210419 and No. 16200220).

APPENDIX A: GRID INDEPENDENCE CHECK

A grid independence check is performed on the symmetric, asymmetric and semiwavy channels using the dimensionless streamwise velocity profile at a specific x location. For the symmetric channel [Fig. 9(a)], a line probe is used to record the streamwise velocity component at $x = L/2$ for $\mathrm{Re} = 670$ with three different grids, where the number in brackets indicates the cell count: G_1 (0.49×10^4), G_2 (1.69×10^4), and G_3 (2.21×10^4). From Fig. 9(a), we find a maximum difference of 8.14% between G_1 and G_2, and of 0.59% between G_2 and G_3. Therefore, G_2 is chosen for our simulations of the flow in the symmetric channel. For the asymmetric channel [Fig. 9(b)], a line probe is used to record the streamwise velocity component at $x = 3L/8$ for $\mathrm{Re} = 570$ with three different grids: G_4 (0.69×10^4), G_5 (2.31×10^4), and G_6 (4.56×10^4). From Fig. 9(b), we find a maximum difference of 8.54% between G_4 and G_5, and of 0.31% between G_5 and G_6. Therefore, G_5 is chosen for our simulations of the flow in the asymmetric channel. For the semiwavy channel [Fig. 9(c)], a line probe is used to record the streamwise velocity component at $x = L/2$ for $\mathrm{Re} = 900$ with three different grids: G_7 (0.41×10^4), G_8 (1.78×10^4), and G_9 (3.25×10^4). From Fig. 9(c), we find a maximum difference of 10.27% between G_7 and G_8, and of 0.52% between G_8 and G_9. Therefore, G_8 is chosen for our simulations of the flow in the semiwavy channel.

Figure 10 shows the computational domain, where grid G_2, G_5, and G_8 are used, respectively, for the symmetric [Fig. 10(a)], asymmetric [Fig. 10(b)], and semiwavy [Fig. 10(c)] channels. The maximum value of y^+ is approximately 0.18.

APPENDIX B: VALIDATION OF THE NUMERICAL FRAMEWORK

To validate our numerical framework, we compare in Fig. 11 the streamlines computed in our simulations with those reported by Harikrishnan *et al.* [9]. Comparisons at both $\mathrm{Re} = 200$ [Figs. 11(a) and (b)) and $\mathrm{Re} = 280$ [Fig. 11(c) and (d)) show that the locations of flow separation and reattachment match well between our simulations and those by Harikrishnan *et al.* [9]. Figure 12 compares our nondimensional z-vorticity contours, $\omega_z H/u_0$, with those reported by Harikrishnan *et al.* [9] at $\mathrm{Re} = 220$ [Figs. 12(a) and 12(b)] and $\mathrm{Re} = 260$ [Figs. 12(c) and 12(d)]. Again, good agreement is found, demonstrating the reliability of our numerical framework.

[1] Z. Mansouri, A novel wavy microcombustor for micro-thermophotovoltaic applications, Chem. Eng. Process. Process Intensif. **163**, 108371 (2021).

[2] Z. Mansouri, Combustion in wavy micro-channels for thermo-photovoltaic applications–part I: Effects of wavy wall geometry, wall temperature profile and reaction mechanism, Energy Convers. Manage. **198**, 111155 (2019).

[3] G. Hunt, N. Karimi, and A. Mehdizadeh, Intensification of ultra-lean catalytic combustion of methane in microreactors by boundary layer interruptions–a computational study, Chem. Eng. Sci. **242**, 116730 (2021).

[4] K. X. Cheng, Z. H. Foo, and K. T. Ooi, Heat transfer enhancement through periodic flow area variations in microchannels, Int. Commun. Heat Mass Transfer **111**, 104456 (2020).

[5] K. Nilpueng, H. S. Ahn, D.-W. Jerng, and S. Wongwises, Heat transfer and flow characteristics of sinusoidal wavy plate fin heat sink with and without crosscut flow control, Int. J. Heat Mass Transfer **137**, 565 (2019).

[6] K. Nilpueng, T. Keawkamrop, H. S. Ahn, and S. Wongwises, Effect of chevron angle and surface roughness on thermal performance of single-phase water flow inside a plate heat exchanger, Int. Commun. Heat Mass Transfer **91**, 201 (2018).

[7] M. Nazeer, M. Irfan, F. Hussain, and I. Siddique, Entropy generation analysis in blood-gold Casson nanofluid through horizontal wavy channel with velocity and thermal slips: Applications in skin diseases, J. Comput. Biophys. Chem. **22**, 259 (2023).

[8] K. S. Mekheimer and Y. A. Elmaboud, The influence of a micropolar fluid on peristaltic transport in an annulus: Application of the clot model, Appl. Bionics Biomech. **5**, 13 (2008).

[9] S. Harikrishnan, P. Kumar, and S. Tiwari, Flow transition in periodically fully developed wavy channels, Phys. Fluids **33**, 073605 (2021).

[10] J. Gollub and S. Benson, Many routes to turbulent convection, J. Fluid Mech. **100**, 449 (1980).

[11] S. Newhouse, D. Ruelle, and F. Takens, Occurrence of strange axiom A attractors near quasiperiodic flows on t^m, $m \geqslant 3$, Commun. Math. Phys. **64**, 35 (1978).

[12] J. P. Eckmann, Roads to turbulence in dissipative dynamical systems, Rev. Mod. Phys. **53**, 643 (1981).

[13] A. Guzmán and C. Amon, Transition to chaos in converging–diverging channel flows: Ruelle-Takens-Newhouse scenario, Phys. Fluids **6**, 1994 (1994).

[14] M. Sarkar and A. Sharma, Fully-developed flow in a furrowed wavy channel: Characterization of unsteady flow regimes and its effect on thermal-hydraulic performance, Numer. Heat Transfer, Part A **68**, 638 (2015).

[15] X. Zhu, J. H. Walther, D. Zhao, and F. Haglind, Transition to chaos in a cross-corrugated channel at low Reynolds numbers, Phys. Fluids **31**, 114107 (2019).

[16] M. J. Feigenbaum, Quantitative universality for a class of nonlinear transformations, J. Stat. Phys. **19**, 25 (1978).

[17] F. Huhn and L. Magri, Stability, sensitivity and optimisation of chaotic acoustic oscillations, J. Fluid Mech. **882**, A24 (2020).

[18] J. R. Mboupda Pone, V. Kamdoum Tamba, G. H. Kom, and A. B. Tiedeu, Period-doubling route to chaos, bistability and antimononicity in a jerk circuit with quintic nonlinearity, Int. J. Dyn. Control **7**, 1 (2019).

[19] A. Libchaber, From chaos to turbulence in Bénard convection, Proc. R. Soc. London A **413**, 63 (1987).

[20] Y. Pomeau and P. Manneville, Intermittent transition to turbulence in dissipative dynamical systems, in *Universality in Chaos* (Routledge, Oxford, 2017), pp. 327–335.

[21] R. C. Hilborn *et al.*, *Chaos and Nonlinear Dynamics: An Introduction for Scientists and Engineers* (Oxford University Press on Demand, Oxford, 2000).

[22] S. V. Patankar, C. H. Liu, and E. M. Sparrow, Fully developed flow and heat transfer in ducts having streamwise-periodic variations of cross-sectional area, Trans. ASME **99**, 180 (1977).

[23] S. W. Gepner and J. M. Floryan, Flow dynamics and enhanced mixing in a converging–diverging channel, J. Fluid Mech. **807**, 167 (2016).

[24] M. Greiner, R. Chen, and R. Wirtz, Enhanced heat transfer/pressure drop measured from a flat surface in a grooved channel, J. Heat Transfer **113**, 498 (1991).

[25] T. Nishimura, Y. Ohori, and Y. Kawamura, Flow characteristics in a channel with symmetric wavy wall for steady flow, J. Chem. Eng. Jpn. **17**, 466 (1984).

[26] T. Nishimura, K. Yano, T. Yoshino, and Y. Kawamura, Occurrence and structure of Taylor–Görtler vortices induced in two-dimensional wavy channels for steady flow, J. Chem. Eng. Jpn. **23**, 697 (1990).

[27] J. Shirani and W. C. Roberts, Clinical, electrocardiographic and morphologic features of massive fatty deposites (lipomatous hypertrophy) in the atrial septum, J. Am. Coll. Cardiol. **22**, 226 (1993).

[28] S. Harikrishnan and S. Tiwari, Simulation of fully developed flow and heat transfer in wavy channels using OpenFOAM, in *Advances in Mechanical Engineering: Select Proceedings of ICRIDME 2018* (Springer, New York, 2020), pp. 869–877.

[29] E. Stalio and E. Nobile, Direct numerical simulation of heat transfer over riblets, Int. J. Heat Fluid Flow **24**, 356 (2003).

[30] E. Stalio and M. Piller, Direct numerical simulation of heat transfer in converging-diverging wavy channels, J. Heat Transfer **129**, 769 (2007).

[31] A. K. Saha and S. Acharya, Turbulent heat transfer in ribbed coolant passages of different aspect ratios: Parametric effects, J. Heat Transfer **129**, 449 (2007).

[32] A. G. Ramgadia and A. K. Saha, Characteristics of fully developed flow and heat transfer in channels with varying wall geometry, J. Heat Transfer **136**, 021703 (2014).

[33] H. G. Weller, G. Tabor, H. Jasak, and C. Fureby, A tensorial approach to computational continuum mechanics using object-oriented techniques, Comput. Phys. **12**, 620 (1998).

[34] H. Jasak, A. Jemcov, Z. Tukovic *et al.*, OpenFOAM: A C++ library for complex physics simulations, in *International Workshop on Coupled Methods in Numerical Dynamics* (IUC, Dubrovnik, Croatia, 2007), Vol. 1000, pp. 1–20.

[35] F. Takens, Detecting strange attractors in turbulence, in *Dynamical Systems and Turbulence, Lecture Notes in Mathematics*, Vol. 898, edited by D. Rand and L. Young (Springer-Verlag, New York, NY, USA, 1981) pp. 366–381.

[36] A. M. Fraser and H. L. Swinney, Independent coordinates for strange attractors from mutual information, Phys. Rev. A **33**, 1134 (1986).

[37] L. Cao, Practical method for determining the minimum embedding dimension of a scalar time series, Physica D **110**, 43 (1997).

[38] L. K. B. Li and M. Juniper, Lock-in and quasiperiodicity in hydrodynamically self-excited flames: Experiments and modelling, Proc. Combust. Inst. **34**, 947 (2013).
[39] S. Balusamy, L. K. B. Li, Z. Han, M. P. Juniper, and S. Hochgreb, Nonlinear dynamics of a self-excited thermoacoustic system subjected to acoustic forcing, Proc. Combust. Inst. **35**, 3229 (2015).
[40] P. Grassberger and I. Procaccia, Characterization of strange attractors, Phys. Rev. Lett. **50**, 346 (1983).
[41] L. K. B. Li and M. P. Juniper, Lock-in and quasiperiodicity in a forced hydrodynamically self-excited jet, J. Fluid Mech. **726**, 624 (2013).
[42] Y. Guan, V. Gupta, and L. K. B. Li, Intermittency route to self-excited chaotic thermoacoustic oscillations, J. Fluid Mech. **894**, R3 (2020).
[43] R. Sujith and S. A. Pawar, *Thermoacoustic Instability: A Complex Systems Perspective*, Springer Series in Synergetics (Springer, Cham, 2021).
[44] J. Ye, H. Li, and J. G. McInerney, Period-doubling route to chaos in a semiconductor laser with weak optical feedback, Phys. Rev. A **47**, 2249 (1993).
[45] P. W. Hammer, N. Platt, S. M. Hammel, J. F. Heagy, and B. D. Lee, Experimental observation of on-off intermittency, Phys. Rev. Lett. **73**, 1095 (1994).
[46] U. Margull, J. Spangler, and W. Prettl, Intermittent breakdown of current-oscillation tori in n-type GaAs epitaxial layers, Phys. Rev. B **50**, 14166 (1994).
[47] M. Frank and M. Schmidt, Time series investigations on an experimental system driven by phase transitions, Phys. Rev. E **56**, 2423 (1997).
[48] W. Just, *Deterministic Chaos: An Introduction* (Wiley VCH, Berlin, 2005).
[49] Y. Xiao, Y. Wang, and Y. C. Lai, Dependence of intermittency scaling on threshold in chaotic systems, Phys. Rev. E **80**, 057202 (2009).
[50] K. Klimaszewska and J. J. Żebrowski, Detection of the type of intermittency using characteristic patterns in recurrence plots, Phys. Rev. E **80**, 026214 (2009).
[51] L. Kabiraj and R. Sujith, Nonlinear self-excited thermoacoustic oscillations: intermittency and flame blowout, J. Fluid Mech. **713**, 376 (2012).
[52] V. R. Unni and R. Sujith, Flame dynamics during intermittency in a turbulent combustor, Proc. Combust. Inst. **36**, 3791 (2017).
[53] J. Y. Huang and J. J. Kim, Type-II intermittency in a coupled nonlinear oscillator: Experimental observation, Phys. Rev. A **36**, 1495 (1987).
[54] E. Ringuet, C. Rozé, and G. Gouesbet, Experimental observation of type-II intermittency in a hydrodynamic system, Phys. Rev. E **47**, 1405 (1993).
[55] S. Chatterjee and A. K. Mallik, Three kinds of intermittency in a nonlinear mechanical system, Phys. Rev. E **53**, 4362 (1996).
[56] J. Sacher, W. Elsässer, and E. O. Göbel, Intermittency in the coherence collapse of a semiconductor laser with external feedback, Phys. Rev. Lett. **63**, 2224 (1989).
[57] P. Ashwin and M. Timme, Unstable attractors: Existence and robustness in networks of oscillators with delayed pulse coupling, Nonlinearity **18**, 2035 (2005).
[58] I. C. Waugh and M. P. Juniper, Triggering in a thermoacoustic system with stochastic noise, Int. J. Spray Combust. Dyn. **3**, 225 (2011).
[59] B. Eckhardt, T. M. Schneider, B. Hof, and J. Westerweel, Turbulence transition in pipe flow, Annu. Rev. Fluid Mech. **39**, 447 (2007).
[60] L. Biferale, M. Buzzicotti, and M. Linkmann, From two-dimensional to three-dimensional turbulence through two-dimensional three-component flows, Phys. Fluids **29**, 111101 (2017).
[61] R. L. Panton, *Incompressible Flow* (Wiley, New York, 2006).
[62] I. Borazjani and F. Sotiropoulos, Vortex-induced vibrations of two cylinders in tandem arrangement in the proximity-wake interference region, J. Fluid Mech. **621**, 321 (2009).
[63] M. Sano and K. Tamai, A universal transition to turbulence in channel flow, Nat. Phys. **12**, 249 (2016).
[64] A. M. Akbarzadeh and I. Borazjani, Large eddy simulations of a turbulent channel flow with a deforming wall undergoing high steepness traveling waves, Phys. Fluids **31**, 125107 (2019).
[65] H. Xia and N. Francois, Two-dimensional turbulence in three-dimensional flows, Phys. Fluids **29**, 111107 (2017).